Spatially unique Shh-Fgf8 distribution in regenerating limb guarantees consistent limb morphogenesis in different limb sizes and contributes to axolotl specific digit patterning.

Saya Furukawa[1], Sakiya Yamamoto[1], Rena Kashimoto[2], Yoshihiro Morishita[3], Akira Satoh[2,4*]

Affiliations:

[1] Okayama University, Faculty of Science, Department of Biological Sciences, Okayama, Japan

[2] Okayama University, Graduate School of Natural Science and Technology, Okayama, Japan

[3] Laboratory for Developmental Morphogeometry, RIKEN Center for Biosystems Dynamics Research, Japan

[4] Research Core for Interdisciplinary Sciences (RCIS), Okayama University, Okayama, Japan

*Corresponding author. Email: satoha@cc.okayama-u.ac.jp

Abstract:

Limb regeneration in *Ambystoma mexicanum* occurs in various sizes of fields and can recreate consistent limb morphology. It was not known what mechanism supports such stable limb morphogenesis regardless of size. Limb regeneration in urodele amphibians has been basically considered to recapitulate the limb developmental processes. Many molecules in the limb developmental processes are conserved with other tetrapods. SHH and FGF8 play important roles in the morphogenesis of limbs among them. Focusing on these two factors, we investigated the detailed expression pattern of *Shh* and *Fgf8* in the various sizes of blastema in axolotl limb regeneration. *Fgf8* is expressed in the anterior side of a blastema and *Shh* is expressed in the posterior side. These are maintained in a mutually dependent manner. We also clarified that the size of *Shh* and *Fgf8* expression domains were scaled as the size of the blastemas increased. However, it was found that the secretion and working range of SHH were kept constant. We also found that the consistent SHH secretion range contributed to promoting cell proliferation and the first digital cartilage differentiation near the *Shh* expression domain. This would be a reasonable system to guarantees constant limb morphogenesis regardless of the blastema size. We also showed that the *Shh-Fgf8* expression domain was shifted posteriorly as the digital differentiation progressed. Consistently, slowing the timing of blocking *Shh* signaling resulted in morphological defects that could be observed in only posterior digits. The revealed posteriorly shifting *Shh-Fgf8* domain might explain urodele specific digit formation, in which digits are added posteriorly.

One-Sentence Summary: A unique SHH-FGF8 spatial interaction compensates for robust limb patterning in regeneration in various limb sizes.

Introduction

Urodele amphibians have the ability to regenerate at the organ level. In contrast, amniotes, including humans, have poor regeneration ability. Numerous studies have sought to clarify the mechanisms for the differences in the regeneration ability between urodele amphibians and amniotes. Among them, limb regeneration has been the most selected to study the superior regeneration ability in urodele amphibians.

Limb regeneration accompanies the formation of a regeneration-specific structure called a regeneration blastema. A blastema consists of many undifferentiated cells called blastema cells, some of which are multipotent and some monopotent [1, 2]. Recent and classic studies indicate that the heterogeneous blastema cell population exhibits similar features and gene profiles to cells in developing limb buds [3, 4, 5, 6]. The ability to form a blastema is one apparent difference between regeneration-competent and -incompetent animals. As such, the mechanism of blastema formation has been well studied. Historically, the presence of nerves in the blastema induction phase has been focused [7]. The essential role of nerves in blastema induction was first demonstrated in 1823 by Todd [7]. Clarification of the entity molecules of the nerves in blastema induction was sought for a long time. Recently, the combined application of FGF2, FGF8, and BMP7 (or BMP2) was proven to substitute for the nerve roles in blastema induction, [8] and these genes are expressed in the nerve cells [9]. The identified genes can induce organ-level regeneration in multiple organs and multiple species [10]. It is of note that the combined activities of FGFs and BMP are necessary to induce a well-patterned limb in axolotl limb regeneration [8]. Either solo FGF input or solo BMP input resulted in a blastema or blastema-like formation, and the induced structure regressed in the end [8]. The co-operative inputs of FGF- and BMP-signaling can induce blastema formation, leading to a patterned limb.

A patterned limb is re-created from a blastema and the patterning mechanisms have been considered to be mimicking limb developmental processes. Axolotl limb development has been investigated at the molecular level and the insights become sufficient to compare its process with other tetrapods. Fundamentally, most limb developmental systems are comparative. For example, *Shh* is expressed in the posterior margin of a developing limb bud [11, 12, 13]. The secreted SHH from the margin of the posterior side of a limb bud is received by PTC, which is a SHH receptor and exhibits a relatively wider range of expression domain compared to *Shh* [12]. The posterior-shifted SHH activity regulates the anteroposterior patterning. This anteroposterior patterning controlled by SHH is believed to be conserved among tetrapods. However, an axolotl-specific limb patterning mechanism has also been revealed. *Fgf8* expression is significantly different from that of amniotes [13, 14]. In amniotes, such as chicks and mice, *Fgf8* expression is restricted to the limb ectoderm during limb development [15, 16]. The ectodermal region where *Fgf8* is expressed is called the apical ectodermal ridge (AER), and it plays a central role in the proximodistal elongation and patterning of a developing limb bud. However, the *Fgf8* expression domain is observable in the mesenchyme in

axolotl limb buds [14]. How this axolotl-specific gene expression pattern contributes to axolotl limb development remains unknown. In addition to the gene expression pattern, limb patterning also exhibits axolotl specificity. In amniotes, the limb digits are basically formed in a posterior to anterior order [17, 18]. In contrast, axolotls form digits in the reverse order [19]. This digit patterning mechanism has remain unclarified and has been a missing link in evolutionary study. In limb regeneration, these conserved and specific features in limb development are considered to be faithfully recreated in a regenerating blastema. To date, similar gene expression patterns have been reported between a developing limb and a regenerating blastema [6]. Furthermore, it was revealed that a formed axolotl blastema could contribute to limb development when a part of the blastema was grafted into a developing limb bud [5]. This indicates the similar properties between a developing limb bud and a regenerating blastema. In this context, blastema induction can be considered to be a rewinding of the developmental clock.

Although limb regeneration has been considered a recapitulation of limb developmental processes in most processes, there are certainly major differences between them. One of the differences between them should be the size. Limb amputation is performed with limbs that are much larger compared to a developing limb bud. Subsequently, a blastema, which has been considered as a similar structure to a developing limb bud, is formed on the amputation plane. Then, the induced blastema undergoes limb morphogenesis. Thus, the field of morphogenesis in limb regeneration is much larger than that in limb development. According to the variation in field size, gene expression should be adapted to the size. However, gene expression in varied field sizes has not yet been investigated in detail.

In the present study, we focused on the axolotl-specific gene expression pattern in varied blastema sizes. Our findings suggest that the gene expression patterns specific to urodele amphibians play an important role in supporting the successful limb regeneration that occurred in a variety of sizes. We also suggest that urodele amphibian–specific gene expression patterns can also explain their specific digit morphogenesis, in which anterior digits are formed prior to posterior digits. These results provide a new perspective on the regenerative capacity of urodele amphibians and contribute to clarifying digit morphogenesis in terms of evolutionary study.

Results

Measurement of the regeneration field in axolotl limbs

Axolotls can regenerate their limbs regardless of their size and age, although nutritional conditions severely affect the regeneration ability. In laboratory conditions, limb regeneration is usually observable in a variety of animal sizes (Fig. 1A–C). Larger animals take a longer time to complete limb regeneration, and smaller animals take a shorter time (Fig. 1A–C). This variation in timing and size makes determination of the blastema stage difficult. In this study, we determined the blastema stage based on blastema appearance, characterizing a late blastema by dorsoventral flattening and a ratio of anterior–posterior to proximal–distal length of approximately 1:1. The outlines of each limb and blastema are shown in Fig. 1D to compare the size. Though there are differences in regeneration time, axolotls can regenerate their limbs throughout their life.

Next, we histologically compared blastemas of different sizes. For experimental convenience, we selected small- and medium-sized animals for most experiments. We obtained similar histological results in both sections, but identified a few differences. The blastemas that grew in medium-size animals (BL-M) exhibited the low-cell density in the anterior and posterior regions (Fig. 1F, asterisks). The blastema epithelium of BL-M tended to be thicker than that in the blastema of small-size animals (BL-S) (Fig. 1E, F). We also compared the cell size in BL-S and BL-M using flow cytometry (Fig. 1G). Blastemas were enzymatically digested and then underwent flow cytometric analysis directly. The signal of the forward scatter (FSC) of the flow cytometry results indicates cell size. Within the nucleated population ($PM2^+$), the plots from BL-M and BL-S were distributed in the same areas. The similarity of the cell size in BL-M and BL-S was also confirmed on the sections, in which the outlines of the cells were visualized by phalloidin rhodamine (Fig. 1H, I). These suggest that the cell size was consistent throughout their life. Based on those fundamental observation, we next focused on the gene expression in different sizes of blastemas.

Shh and Fgf8 expression domains in different blastema sizes

We next investigated how genes were expressed in blastemas of different sizes. *Shh* and *Fgf8* expression patterns were investigated by *in situ* hybridization since *Shh* and *Fgf8* are known to play an essential role in limb patterning in many animals (Fig. 2). In BL-S, *Shh* was typically expressed locally at the margin of the posterior mesenchyme along the blastema epidermis (Fig. 2A, B). In BL-M, *Shh* expression appears to be regulated differently at the proximodistal level. In the distal region of BL-M, the Shh^+ domain was restricted in the posterior margin (Fig. 2F). The Shh^+ domain of the proximal side was, however, apart from the posterior margin of the blastema epithelium (Fig. 2E, F). It is of note that the disconnection of the Shh^+ domain from the posterior margin is a characteristic expression pattern. *Fgf8* was expressed in the anterior side of the blastema mesenchyme as described [13](Fig. 2C, D, G, H). As shown in Fig. 2C and G, *Fgf8* was expressed in

the anterodorsal and anteroventral blastema mesenchyme. The longitudinal sections were prepared with a slight deviation from the midline due to this characteristic *Fgf8*$^+$ domain (Fig. 2A, C, E, G). The detachment of the *Fgf8*$^+$ domain from the anterior margin was commonly observed (Fig. 2C, G, 3D). To describe the *Shh*$^+$ and *Fgf8*$^+$ domain in more detail, a three-dimensional (3D) reconstitution was performed (Fig. 2I, J). Two sets of serial sections, one each for *Shh* and *Fgf8*, underwent regular *in situ* hybridization procedures. Then, all sections were captured and reconstituted into 3D animation. In the very distal region of the blastema, *Fgf8* was expressed throughout the blastema mesenchyme and no *Shh* expression was observed (Fig. 2I, J, Supplemental Mov. 1). The *Shh*$^+$ domain was observable from the sub-distal region. The spatial distribution of the *Shh*$^+$ and *Fgf8*$^+$ domain in various size of blastemas is basically smiliar but also exhibits some differences.

To investigate further, we measured the *Shh*$^+$ and *Fgf8*$^+$ domain in the transverse sections of the blastema (Fig. 3). The measuring scheme is described in Sup. Fig. 1A and B. As described, the *Shh*$^+$ domain was varied at the proximodistal level (Fig. 2F, Supplemental Mov. 1). To normalize this variation, we selected two or three sections from an identical blastema, on which *Shh* and *Fgf8* expression could be confirmed, and its average was calculated. The average widths are aligned and presented graphically in Fig. 3A and D. (The raw data is shown in Sup. Fig. 1C and D.) The *Shh*$^+$ domains were located on the posterior side. As illustrated in Fig. 2, the *Shh*$^+$ domain tends to be apart from the posterior end of the blastema mesenchyme in larger blastemas. The scatter diagram of the width of the *Shh*$^+$ domain and the blastema width shows the clear correlation (R = 0.8248) between them (Fig. 3B). Focusing on the occupation ratio of the *Shh*$^+$ domain in the blastema, the ratio of the *Shh*$^+$ domain was relatively constant, at an average of 22.8%. (Fig. 3C). No difference in the *Shh*$^+$ domain between the forelimb and the hind limb could be found (Fig. 3B, C). As for the *Fgf8*$^+$ domain, the *Fgf8*$^+$ domain was wider than the *Shh*$^+$ domain and was located on the anterior side of the blastemas (Fig. 3D). The *Fgf8*$^+$ domain was much weakly correlated with the blastema with as compared to the *Shh*$^+$ domain (Fig. 3E). On the other hand, it was observed that the range of *Fgf8* expression relative to the size of the regenerating blastemas tended to be constant regardless of size, although there was a larger variation as compared to the *Shh*$^+$ domain (Fig. 3F). Lastly, we aligned the *Shh*$^+$ and *Fgf8*$^+$ domains on the adjacent sections (Fig. 3G). On most sections, the *Shh*$^+$ and *Fgf8*$^+$ domains were not merged and a certain distance existed between the two expression domains (Fig. 3G). Those results indicate the expression domain of *Shh* and *Fgf8* are scaled along with the blastema size.

Next, we investigated how the distribution of secreted factors was affected by gene expression that is scaled along with blastema size, focusing on *Shh*, which plays a major role in the anteriorposterior limb patterning. The *Ptc1* gene encodes a receptor for SHH and its expression has been used as an indicator of the SHH distribution [22, 23]. *Shh* is expressed in the posterior margin of an amniote limb bud and SHH is secreted toward the anterior side, creating an SHH gradient in the limb

bud [20, 21]. As in the amniote limb bud, *Ptc1* was found in the posterior side of the BL-S and BL-M (Fig. 4B, D). The *Ptc1*$^+$ domain was overlapped with the *Shh*$^+$ domain and extended to the anterior, forming a relatively wider expression domain compared to the *Shh*$^+$ domain (Fig. 4A–D). As with the *Shh*$^+$ domain, the *Ptc1*$^+$ domain width exhibits a correlation with the blastema width (R = 0.7557, Fig. 4E), and the ratio shows consistency (Fig. 4F, average = 40.3%). No apparent differences in the *Ptc1*$^+$ domain between the forelimbs and the hind limbs were observed. To estimate SHH diffusion, the extent of *Ptc1* expression was investigated. *Ptc1* expression has been used as an indicator of SHH diffusion in limb developmental studies[22, 23]. The lines were drawn at the anterior limits of the *Ptc1*$^+$ and *Shh*$^+$ domains, respectively. Next, the width of these two lines (the anterior borders of the *Shh*$^+$ and *Ptc1*$^+$ domains) was calculated and defined as the SHH diffusion range (Fig. 4G, H). The SHH diffusion range was constant, suggesting the same distribution of SHH from the anterior border of the *Shh*$^+$ domain, regardless of blastema size. This constant SHH-diffusion range was also supported by simulations. We simulated the spatial distributions of SHH in tissues with two different sizes of *Shh*$^+$ domains using a mathematical model for SHH diffusion and degradation (Fig. 4I–K). It was assumed that all cells have the same expression level and secretion rate of SHH in the expression domain. The curves in the figures show the results for different degradation rates. To compare the SHH diffusion ranges between the cases with different sizes of *Shh*$^+$ domains, the spatial patterns of SHH were shifted in parallel so that the anterior ends of expression domains coincide (Fig. 4K). It was found that the SHH diffusion range was very similar, independent of its expression domain size, although the difference was slightly clearer when the degradation rate was smaller. Those strongly suggest that the working range of SHH is constant regardless of the size of the *Shh*$^+$ domain and the size of blastemas.

Shh and Fgf8 regulation and functions in regenerating blastemas

Next, we focused on the relationship between *Shh* and *Fgf8* expression in a regenerating blastema (Fig. 5). In amniotes, *Shh* expression is maintained by *Fgfs* secreted from the AER [24]. As above, *Fgf8*, which is expressed in the AER in amniotes, is expressed in the blastema mesenchyme. To investigate the interaction between *Shh* and *Fgf8* in the blastema mesenchyme, chemical compounds were used to inhibit the signaling cascades. Cyclopamine was used to inhibit SHH signaling and SU5402 was used to inhibit FGF signaling (Fig. 5). For the inhibitor treatment, we used smaller animals (5 cm). Animals that were 7 days post amputation were used, and then we kept the animals in chemical-containing water for 3 days. In the control (DMSO-treated animals), *Shh*, *Fgf8*, *Ptc1*, and *Col1a* expressions were observable (Fig. 5A, top row). Cyclopamine-treated animals exhibited no signals of *Shh*, *Fgf8*, or *Ptc1*, although *Col1a* expression, as a positive control, could be detected (Fig. 5A, mid row). In the SU5402-treated blastemas, the signals of *Shh*, *Fgf8*, and *Ptc1* as well as *Col1a* could be found. (Fig. 5A, bottom row). For further analysis, we also performed

quantitative reverse transcription polymerase chain reaction (RT-PCR) (Fig. 5B). The blastemas were harvested from the animals, which were treated as above. *Shh* and *Fgf8* expression levels were investigated in the blastemas. Cyclopamine or SU5402 treatment decreased both the *Fgf8* and *Shh* expression level (Fig. 5B). These results suggest that positive feedback exists between *Shh* and *Fgf8* expression in a regenerating blastema. Although the *Fgf8* expression is in the mesenchyme, the positive relationship between *Shh* and *Fgf8* might contribute to the maintenance of their expression domains in the posterior and anterior regions of the blastema, respectively.

The function of FGF8 and SHH in a developing limb bud has been described previously [25, 26]. In amniotes, FGF8 or SHH was shown to have mitogenic activity in developing axolotl limb buds [25, 26]. However, the mitogenic activity of SHH and/or FGF8 in a regenerating axolotl blastema remains unknown. Accordingly, the mitogenic effects of SHH and FGF8 on blastema cells were assessed (Fig. 5C). We cultured axolotl blastema mesenchymal cells and treated them with SHH and/or FGF8 for 3 days. The *proliferating cell nuclear antigen* (*Pcna*) expression level was measured by quantitative RT-PCR (Fig. 5C). In our culture system, SHH or FGF8 alone showed statistically significant (*p* values are represented as follows: ***< 0.01. *<0.05.) *Pcna* upregulation in axolotl blastema cells compared to the control. Furthermore, combined treatment with SHH and FGF8 produced much higher upregulation of *Pcna* in axolotl blastema cells than SHH or FGF8 single treatment. This suggests that the cells under the influence of both FGF8 and SHH have better advantages in cell proliferation in a regenerating blastema.

Next, we investigated whether the mitogenic activity of FGF8 and SHH had an influence on cell density in a blastema. The gene expression pattern of *Fgf8* and *Shh* was found in the anterior and the posterior region, respectively. Thus, the intermediate region between the *Fgf8*$^+$ and the *Shh*$^+$ domain would be the area strongly influenced by both FGF8 and SHH. Next, we explored the positional relationship between cell density and *Shh* expression (Fig. 6). First, *Shh* expression was visualized by section *in situ* hybridization, and then the section was compartmentalized into a 100 μm square by Photoshop CS6 software (Fig. 6A). All cells were counted and all *Shh*$^+$ cells were marked based on the Hoechst signal. Then, the cell density was visualized (Fig. 6B). The aligment between the samples was performed at the anterior end of the *Shh*$^+$ cell–containing square. The alignment of the data clarifies that the higher cell density squares were located around the anterior border of the *Shh*$^+$ domain. To evaluate this in a 3D manner, the sections were resonsitututed in AMIRA software (Fig. 6C–F, Supplemental Mov. 2–4). Briefly, blastemas were fixed and sectioned. Then, the sections underwent *in situ* hybridization to visualize *Shh* expression. Pictures of all sections from the tip to the bottom were taken and processed into stack data with a semi-auto alignment. The nuclei of the blastema mesenchyme were plotted manually based on the Hoechst signal, and the 3D address was obtained. Based on the acquired 3D address, the 3D image was reconstituted. We also marked the *Shh*$^+$ cell and displayed it in pink (Fig. 6C, E, Supplemental Mov.

2). Cell density was calculated as the average distance from the five nearest nuclei (Fig. 6D, F, Supplemental Mov. 3, 4). The density of the cells tends to be higher near the *Shh* expression domain. To visualize the cell density on a X-Y plane, we extracted three images from the proximal region and show the merged image in the proximal view (Fig. 6E, F, Supplemental Mov. 4). Visualizing the 10 cells with the highest cell density, they are concentrated in roughly two areas of the regenerating blastema (Fig. 6F, arrows). One of the two areas, located near the *Shh*$^+$ domain, appears to have higher density compared to the other area. Given the *Shh* and presumptive *Fgf8* expression pattern, the area showing relatively higher cell density near the *Shh*+ domain would be exposed by both SHH and FGF8. Therefore, this is consistent with the synergic mitogenic activity of SHH and FGF8.

Digit formation by the relationship between Shh and Fgf8

Lastly, we examined how to maintain the robustness of limb morphogenesis regardless of blastema size. The mitogenic activity of SHH and FGF8 likely contributes to the increasing cell density. We hypothesized that the increase in cell density leads to cartilage differentiation since it was shown that higher cell density leads to cartilage differentiation in chicken limb bud culture [27]. First, we investigated gene expression patterns in the regenerating blastema on both longitudinal and transverse sections, in which the first digit started differentiating (Fig. 7). *Shh* and *Ptc1* were used to visualize SHH distribution (Fig. 7A, B, G). *HoxA13* was used to show the presumptive autopod area (Fig. 7C, I), and the forming cartilage element was shown by *Col2a* (Fig. 7D, H). *Fgf8* is visualized only on the transverse sections due to its characteristic dorsoventrally separated expression pattern. The longitudinal sections are adjacent sections, not identical sections. However, based on the boundary between the blastema mesenchymal cells and the epithelium, an approximate merged image was created (Fig. 7E). The merged image shows that the *Col2a*$^+$ area appeared near the *Shh*$^+$ domain within the *HoxA13*$^+$ domain (Fig. 7E). On the transverse sections, the *Col2a*$^+$ region appeared between the *Fgf8*$^+$ and *Shh*$^+$ domain within the *HoxA13*$^+$ area (Fig. 7F–I). This suggests that the first digit is induced in the region where is assumed to be exposed both SHH and FGF8.

Next, we tested whether a similar digit formation mechanism also functioned in the more posterior digits. We visualized *Shh* expression after first digit (digit II) formation by *in situ* hybridization. Previous reports demonstrated that *Shh* expression was maintained even after digit I and II formation in axolotl limb development [11, 26]. Consistently, *Shh* expression was confirmed in the blastema after digit II formation (Fig. 8A, A’, C, C’ E). *Fgf8* expression was also investigated and found on the adjacent section (Fig. 8B, B’, E). The *Col2a*$^+$ domain became larger compared to that in Fig. 7H (Fig. 8C, C’) due to the growth of cartilage as the regeneration stage progressed. *HoxA13* expression indicates that expressions of *Shh*, *Fgf8*, and *Col2a* are in an autopodial region (Fig. 8C, D, D’). To focus on the positional relationship of *Shh*, *Fgf8*, and *Col2a* expression, the spatial positions of *Shh*$^+$, *Fgf8*$^+$, and *Col2a*$^+$ cells were plotted, merged from the adjacent section, and projected to the

section showing *Col2a* expression (Fig. 8E). The merged image suggests that *Shh*$^{+}$ cells and *Fgf8*$^{+}$ cells are shifted posteriorly and located in a more posterior region than the digit II region. Next, we investigated the role of the posteriorly shifted *Shh*$^{+}$ domain in posterior digit formation. We applied cyclopamine from various time points and observed the digit pattern (Table 1, Fig. 8F–O). Cyclopamine treatment immediately after limb amputation resulted in spike formation as previously reported whereas DMSO treatment did not induce any defects [28] (Fig. 8F, G). However, when the timing of the cyclopamine treatment was delayed, the digit loss number decreased accordingly (Table 1, Fig. 8H–O). A similar observation can be found in axolotl limb development [29]. These results suggest that sustained SHH activity is required for the posterior digit formation. This also implies that the corresponding posteriorly shifted *Fgf8* to *Shh* expression contributes to increasing cell density and subsequent digit formation in the posterior region.

Discussion

Characteristic expression pattern of Shh and Fgf8 in regenerating limb blastemas

The present study shows that regenerating axolotl limbs have a characteristic *Shh* and *Fgf8* expression pattern during limb regeneration. As in amniotes, *Shh* is expressed in the posterior margin of a developing limb bud, even in axolotls [11]. However, the *Shh* expression pattern in blastemas showed a difference (Fig. 2). The *Shh*$^+$ domain was not necessarily maintained in the margin of the blastema (Fig. 2E, F). A larger blastema tended to show the *Shh* expression pattern with segregation of its proximal side from the blastema epithelium (Fig. 2E, F). This segregated *Shh* expression pattern is quite unique in terms of the reported *Shh* expression patterns of developing limb buds in other species [11, 12, 13]. *Shh* is maintained by FGFs secreted from the AER in amniotes [24]. The *Shh*$^+$ domain restriction to the posterior margin is controlled by *dHand* (*Hand2*), *Tbx2*, *Gremlin*, and *Alx4* [30, 31, 32]. In axolotl limbs, the expression pattern of *Tbx2*, *dHand*, *Alx4*, and *Gremlin* was reported [13, 26, 33]. Among those, no characteristic expression pattern appears to be found as compared to other vertebrates. Only *Fgf8* shows an apparent difference among the genes reported to play roles in *Shh* spatial restriction. *Fgf8* is expressed on the anterior-mesenchymal side [13] (Fig. 2C, D, G, H). It was reported that the mesenchymal *Fgf8* and *Shh* have been demonstrated to have a positive feedback loop via *Gremlin* [13] (Fig. 5A, B). This mesenchymal *Fgf8* expression and the positive interaction of *Fgf8* and *Shh* may account for the unique *Shh* expression domain. As in amniotes, *Shh* is maintained by *Fgf8* but, unlike in amniotes, the *Fgf8*$^+$ domain is on the anterior side. The position of the *Fgf8*$^+$ domain is varied in blastemas, and a larger size provides more space to be positioned from the center to the anterior side of a blastema (Fig. 3D). Actually, *Fgf8*$^+$ domain tended to take more varied position in larger blastemas than smaller ones (Fig. 3D). Given the mutual maintenance (Fig. 5B) and constant SHH diffusion in the different sizes of blastemas (Fig. 4H–K), the anterior shift of the *Fgf8*$^+$ domain leads to an anterior shift of the *Shh*$^+$ domain, resulting in the segregation of the *Shh*$^+$ domain from the posterior margin (Fig. 9A). In smaller blastemas, the SHH diffusion showed quite similar range to larger blastemas. So, the expression region of *Fgf8* is inevitably pushed to the anterior side in smaller blastemas. The expression of *Shh* is also pushed to the rear by the mutually dependent expression maintenance mechanism (Fig. 9A). This mechanism may maintain the expression levels of *Shh* and *Fgf8* at the bilateral margins in smaller blastemas. This characteristic *Shh* and *Fgf8* regulation might contribute to the ability of limb regeneration in blastemas with varied sizes. In other words, the flexible *Shh* and *Fgf8* expression domain but the consistent SHH working distance in axolotl limb regeneration might guarantee consistent morphogenesis in the limb regeneration induced in different sizes of animals.

Cell memory and Shh/Fgf8 expression in axolotl blastema

Blastema cells are derived from fully differentiated tissues. This is one of the biggest

differences between a developing limb bud and a regenerating blastema. Mesenchymal cells of a developing limb bud are derived from undifferentiated cells sources, such as the lateral plate mesoderm. In contrast, blastema cells are induced from differentiated tissues, such as dermis [34]. Cell origin must have a great influence on limb morphogenesis, even though a developing limb bud and a regenerating blastema exhibit similar genetic cascades in morphogenesis. We have previously demonstrated that the gene expression pattern reflects cell origin [35]. *Shh*-expressing cells only emerge from posteriorly derived cells. Thus, it is very likely that *Fgf8*-expressing cells are derived from anterior tissues. This "positional memory" of cells would be unique to limb regeneration compared to limb development. In limb development, it is considered that recognition of a location of a cell is sequentially induced following the developmental program. In contrast, in limb regeneration, the positional memory is in cells before amputation and it is activated after amputation. The entities of the positional memory have not yet been clarified. However, this "pre-determined cellular memory" may be important for limb regeneration. In contrast to limb development, the linages of cells that form a blastema, rather than induction by secreted factors, might contribute more to the determination of spatial coordinates within a blastema. Dermis is a major contributor to a blastema [36]. The quantitative the contribution from dorsal/ventral/anterior/posterior tissues has not yet been carried out. However, it is very likely that the cell contribution from each orientation is varied. Thus, the ratio of blastema cells derived from anterior/posterior tissues may be uneven in each blastema. This may be the cause of the variation in the width of the *Fgf8* expression domain in the blastemas (Fig. 3D). If the contribution of anterior cells to a blastema is large, the anteriorly derived cells will dominate in a blastema. This might lead to posteriorly shifted *Shh*-*Fgf8* expression. Similarly, if the posterior cell contribution is dominant, an anteriorly-shifted *Shh*-*Fgf8* expression would be expected (Fig. 9A). The unique limb morphogenesis accorded by flexible *Shh*-*Fgf8* expression guarantees robust limb regeneration in such a varied cell contribution. Further research is needed to better understand the memory of the orientation and the contribution rate.

Digit specification mechanism regardless of field size

The present study provides evolutionary insights into digit formation. SHH and FGF8 have synergic cell proliferative activity (Fig. 5C). In addition, a higher density of blastema cells could be observed in the area where are assumed to be exposed to both SHH and FGF8 (Fig. 6). Our results also suggest that this area is where the initial digit chondrogenesis occurs (Fig. 7). In evolutionary morphology, the formation of the first digit occurs near the Shh^{+} domain [37]. From this perspective, the mechanism by which the formation of the first digit is induced in the vicinity of the Shh^{+} domain can be considered to be conserved in the axolotl. However, the area affected by SHH and FGF8, which leads to cell proliferation, was shown to be flexible in position within a blastemal (Fig. 3), and gradually shifted posteriorly in the mesenchyme of the axolotl (Fig. 8). The mechanism of this

posterior transition is unknown. However, considering that the number of cells capable of expressing *Shh* is limited to those of posterior origin and that the induced cartilage can be a physical barrier to the diffusion of SHH, a model such as Fig. 9B can be hypothesized. The interdependent relationship between *Shh* and *Fgf8*, which is completed in the mesenchyme, may allow the flexible positioning of *Shh*-*Fgf8* in the mesenchyme. The relationship between the shift of *Fgf8* to the AER and the change in the finger formation mechanism remains unclear. However, if we can understand the mechanism of digit formation caused by the immobilization of the source of FGF8 to AER, it will undoubtedly bring deeper insights into morphological evolution.

Materials and Methods

Animals and Surgery

For most experiments, axolotls (*Ambystoma mexicanum*) with a nose to tail length of 8 to 15 cm obtained from private breeders and housed in aerated water at 22°C were used. A larger animal (25cm) was used to show its regeneration process and smaller animals (5 cm) were used for chemical treatment. Before the all surgeries, axolotls were anesthetized using MS-222 (Sigma Aldrich, St. Louis, Missouri) for about 10 minutes (depending on the animal size). Limbs were amputated at the middle of the zeugopod. All animal usage was approved by the Animal Care and Use Committee, Okayama University (#580 to A.S) and all animal experiments were conducted following the guidelines of Okayama University.

Sectioning and histological staining

Samples were fixed with 4 % paraformaldehyde for 1 day at room temperature and embedded in O.C.T. compound (Sakura Finetek, Tokyo, Japan) following 30% sucrose/PBS treatment for approximately 12 hours. Frozen sections with a thickness of 10 µm were prepared using a Leica CM1850 cryostat (Leica Microsystems, Wetzlar, Germany). The sections were dried under an air dryer and kept at −80°C until use. Standard hematoxylin and eosin (HE) staining was used for histology. To visualize cartilage formation, alcian blue staining was performed before HE staining. In brief, sections were washed in tap water several times to remove the O.C.T. compound. Then, acian blue (Wako, pH 2.0) solution was dropped on the section and the slide was incubated for 2 min. The sections were washed twice with tap water, and then HE staining was performed. The stained sections were mounted using Softmount (Wako).

Flow cytometry

Blastema cells were dispersed using collagenase (Wako Pure Chemical Industries, Osaka, Japan). Filtration was then performed using Cell Strainer (FALCON, 45mm mesh). Cells were suspended in 40% Dulbecco's modified Eagle Medium (gibco), 50% DDW, 10% FCS, 0.01M HEPES, 3µg/mL gentamysin. The cells were then resuspended in PBS. Cells were dissolved in 1 ml of PBS and nuclei were stained with propidium iodide (PI) (Merck Millipore, Burlington, MA, USA) and analyzed using a flow cytometer (Guava PCA). The data were analyzed using FCSalyzer (https://sourceforge.net/projects/fcsalyzer/).

Actin staining

After washing samples with TBST (0.15M NaCl, 0.1M Tris and 0.1% Tween20), Alexa Fluor™ 594 Phalloidin (#A12381, Invitrogen, CA, USA), was added at 1:500 dilution and incubated for 20 minutes at room temperature. Samples were washed with TBST, and nuclei were visualized by

Hoechst33342 (#346-07951, Wako-Fuji film).

in situ hybridization and nuclear visualizing

RNA probes for *Fgf8*, *Shh*, *HoxA13*, *Col1a* and *Col2a* were selected as previously described [1-4]. The axolotl *Ptathed 1* (*Ptc1*) gene was newly isolated. The isolated sequences are from 1016-2989 of AMEX60DD201043057.6 in the axolotl OMICS site (https://www.axolotl-omics.org/). *In situ* hybridization was performed as reported (Satoh et al., 2007). Briefly, samples were treated with protainase K (10μg/ml) at room temperature for 20 min, and riboprobes were hybridized at 62.5°C. Following hybridization, samples were washed with buffer 1 (50% formamide and 5×saline-sodium citrate (SSC)) twice for 20 minutes and buffer 2 (50% formamide and 2×SSC) three times for 20 minutes at 62.5°C. After samples were blocked with 0.5% blocking reagent (#11096176001, Roche) /TBST, an Anti-Digoxigenin-AP, Fab fragments (#11093274910, Roche) was added at 1:1000 dilution and incubated for 2 hours at room temperature. Staining was done with NBT (#148-01991, Wako-Fuji film) and BCIP (#05643-11, Nakarai Tesque) in NTMT (100mM NaCl, 0.1M Tris pH9.5 and 0.1% Tween20). Nuclei were visualized by Hoechst33342 (#346-07951, Wako-Fuji film) after performing *in situ* hybridization. Images were captured using an Olympus (Tokyo, Japan) BX51 fluorescence microscope.

Measurement of the signals on sections

Measurement of gene expression domains was on the software (Cellsense, Olympus). Width of blastema mesenchyme along with anteroposterior axis and gene expression domain were measured using measurement tool on Cellsense. To maintain fairness, all measurements were performed under the same exposure time and magnification.

Simulations for the spatial distribution of SHH

In Figs. 2J-K, we numerically solved the following partial differential equation for diffusion and linear degradation of SHH using Mathematica software (ver. 12.1.1.0).

$$\frac{\partial u(x,t)}{\partial t} = D\frac{\partial^2 u(x,t)}{\partial x^2} - \gamma u(x,t) + f(x),$$

$$f(x) = \begin{cases} \alpha & (0 \le x \le \delta) \\ 0 & (x > \delta) \end{cases},$$

where $u(x,t)$ is the SHH concentration at position x and time t. D and γ are the diffusion constant and degradation rate, respectively, and those values were set so as to $\sqrt{\gamma / D} = 1/200$. δ is the size of SHH expression domain, and we simulated the cases with $\delta = 100\,[\mu\mathrm{m}]$ and

$\delta = 200$ [μm]. α is the secretion rate of SHH, and we set $\alpha = 1.0$ [a.u.]. A Neumann boundary condition, $\partial u / \partial x = 0$, was used at both posterior and anterior ends of a tissue. Regarding tissue size (denoted by L), the cases with $L = 500$ [μm] and $L = 1,000$ [μm] were tested. Figures 2J-K show the spatial distribution of SHH at the steady state.

SU5402 and cyclopamine treatments

Animals were treated with 10mL solutions for all chemical treatments. For this experiment, smaller animals were used (5 cm in length). Working stocks of 30mM SU5402 (#193-16733, Wako) and 8mM Cyclopamine (#C9710, LKT Labs, Inc) were made in DMSO (#08904-14, Nakarai Tesque) and diluted to 30 μM and 8 μM in water. Control animals were treated with a solution containing an equal amount of DMSO. The chemical-containing water was refreshed every day (Figure 5) or every two days (Figure 8).

qRT-PCR analysis

RNA preparation for RT-PCR was performed using TriPure Isolation Reagent (Roche). Reverse transcription was performed using PrimeScript™ II Reverse Transcriptase (Takara). The quantitative RT-PCR analysis was performed by StepOne™ (TermoFisher) and KAPA SYBR FAST qPCR Master Mix (Kapa Biosystems). Primers are described below:

EF1α forward, AACATCGTGGTCATCGGCCAT
EF1α reverse, GGAGGTGCCAGTGATCATGTT
Shh forward, GCTCTGTGAAAGCAGAGAACTCG
Shh reverse, CGCTCCGTCTCTATCACGTAGAA
Fgf8 forward, CGAAGGATGGTACATGGCCT
Fgf8 reverse, TATCGCGGTACGGAATGTCG
Pcna forward, ATGTTTGAGGCTCGCCTGGT
Pcna reverse, GCAGCGGTACGTATCGAAGC

Cell culture and protein addition

Harvested blsatemas were removed the epithelial tissues from blastemas in 1% EDTA/PBS using forceps. Only mesenchyme tissues were used for the cell culture. After washing with PBS, the tissues were broken into smaller pieces. Obtained mesenchyme cells were suspended in culture medium (50% water, 40% GlutaMax-DMEM, 10% FCS and 0.01M HEPES (pH. 7.5), and 300 mg/ml Gentamycin). FGF8 (R&D systems, #423-F8) or/and SHH (R&D systems, #461-SH) proteins were added to the culture medium at a concentration of 0.1 μg/ml. The culture medium was refreshed every day.

3D reconstruction and distance map

Consecutive blastema sections were carried out the *in situ* hybridization and nuclei were visualized by Hoechst33342. Images were captured using an Olympus (Tokyo, Japan) BX51 fluorescence microscope, and they were reconstructed through volume rendering using Amira Software (version 6.4.0, Thermo Fisher Scientific, K.K., Tokyo, Japan; http://www.fei.com/software/amira-3d-for-life-sciences/) running on an iMacPro (CPU: 2.3 GHz Intel Xeon W, DRAM: 128GB 2666 MHz DDR4, and graphics: Radeon Pro Vega 64 16368 MB; Apple Japan, Tokyo). Gene expression domains were extracted using segmentation tool on Amira. Nuclei were marked manually on Amira, and obtained nuclei coordinate information. Nuclei coordinate information was divided into four files due to technical limitation. Distances between nuclei were calculated. The 5 shortest distances were selected and calculated the average of these 5 distances. We found that visualization of the average distance from two to four nuclei was problematic, especially around the blastema margin. In contrast, visualization of the average distance from more than six nuclei looked no different. Thus, we decided to utilize the five nearest nuclei to visualize the cell density. The calculations were performed by a following python script (https://github.com/satohlab-py/cell-density.git; script name = "uptolist"). These calculations were repeated to every divided four files. Obtained four files were connected manually. The average distances were squared to visualize cell density clearly. Subsequently, the nuclei dots were colored depends on the average distance, then the dots were reconstructed to the 3D image. These tasks were performed by a following python script (https://github.com/satohlab-py/cell-density.git; sript name = "uptograph"). These tasks were performed by the Python programming language (Python Software Foundation, https://www.python.org/).

Whole mount alcian blue staining

Samples were fixed with formalin overnight, and replaced in graded ethanol series 25%, 50%, and 70%. Samples were stained with alcian blue in 70% EtOH and 1% HCl for 12 hours. Stained samples were washed with 70% and 100% EtOH.

1. R. Iwata, A. Makanae, A. Satoh, Stability and plasticity of positional memory during limb regeneration in Ambystoma mexicanum. *Developmental dynamics : an official publication of the American Association of Anatomists* **249**, 342 (Mar, 2020).
2. A. Makanae, K. Mitogawa, A. Satoh, Co-operative Bmp- and Fgf-signaling inputs convert skin wound healing to limb formation in urodele amphibians. *Developmental biology* **396**, 57 (Dec 1, 2014).
3. K. Mitogawa, A. Makanae, A. Satoh, A. Satoh, Comparative Analysis of Cartilage Marker Gene Expression Patterns during Axolotl and Xenopus Limb Regeneration. *PloS one* **10**,

e0133375 (2015).

4. A. Satoh, D. M. Gardiner, S. V. Bryant, T. Endo, Nerve-induced ectopic limb blastemas in the Axolotl are equivalent to amputation-induced blastemas. *Developmental biology* **312**, 231 (Dec 1, 2007).

Acknowledgments: We are grateful R. Iwata and T. Satoh for their laboratory work. We thank K. Nishimura for making a prototype of the Python script. Animals were obtained from Hiroshima University Amphibian Research Funding. This work is supported by a JSPS KAKENHI grant-in-aid for scientific research (B) (#20H03264 to AS).

Author contributions: S.F.: investigation, data collection, data analysis, methodology. S.Y.: supportive investigation, writing–review and editing. R.K.: supportive investigation, animal housing, writing–review and editing. Y.M.: simulation, writing. A.S.: investigation, methodology, conceptualization, supervision, writing–review and editing, project administration, funding acquisition.

Competing interests: The authors declare no competing interests.

Data and materials availability: All data are available in the main text or the supplementary materials.

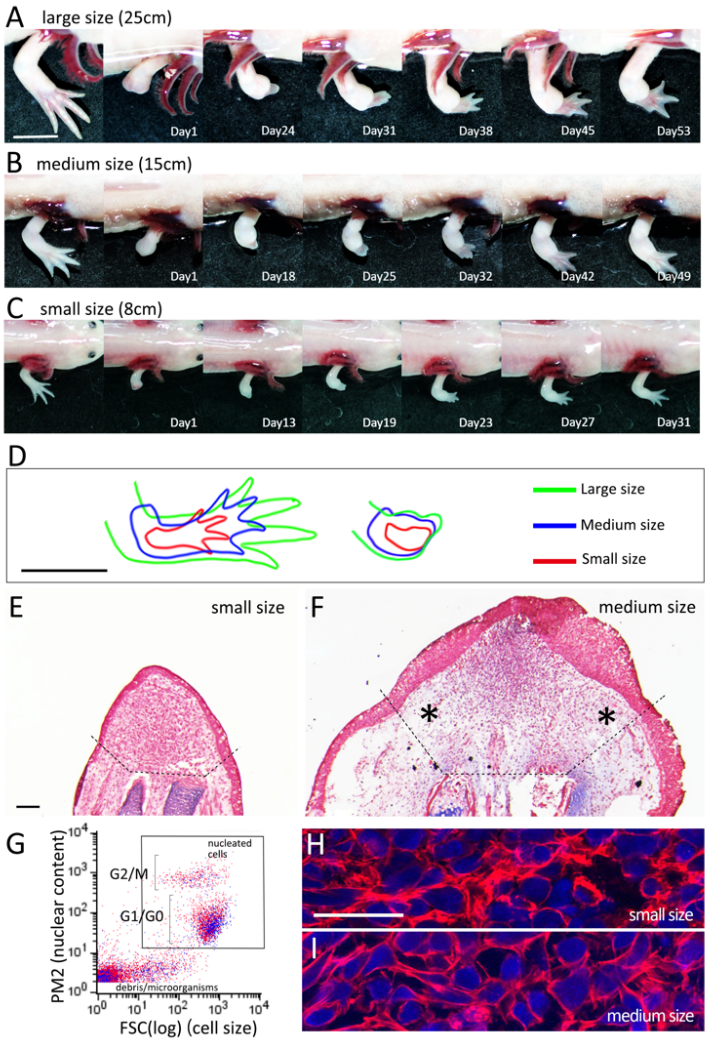

Fig. 1. Limb regeneration at different animal sizes and blastema formation. (A–C) Time course of the limb regeneration process in different size animals. Scale bar in A = 1 cm. (D) The outlines of the limbs and regeneration blastemas shown in A~C. The regeneration blastemas were chosen to have a 1:1 anteroposterior width and proximodistal width at each size. Scale bar in D = 1 cm. (E, F) Alcian, eosin & hematoxylin staining. The dotted lines indicate the presumptive amputation plane. Asterisks indicate the sparse regions. Histological analysis reveals the presence of the sparse region in the larger size of blastema. Scale bar in E = 200 μm. Posterior is to the left. (G) Flow cytometric analysis. The red and the blue dots indicate the blastema cells derived from medium- and small-size animals, respectively. No significant difference in cell size was observed. (H) Phalloidin rhodamine and Hoechst staining. Scale bar in H = 50 μm.

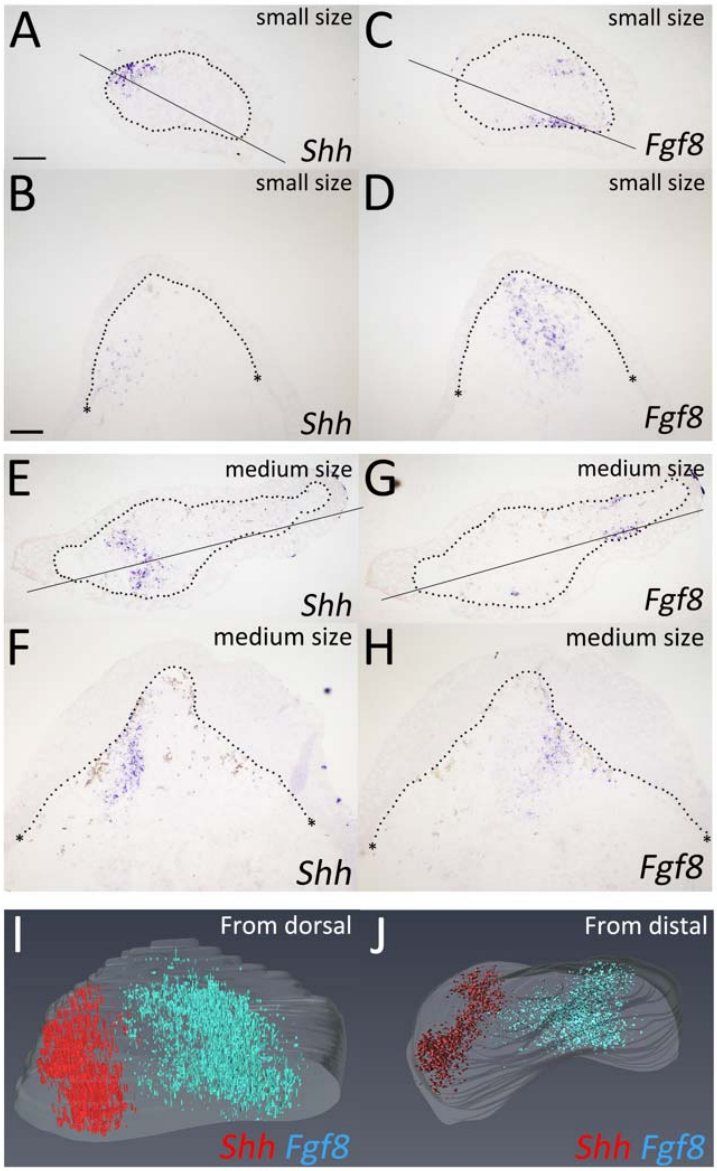

Fig. 2. *Shh* and *Fgf8* expression pattern in the small and the medium size of the blastema. (A–H) *Shh* and *Fgf8* expression was visualized by *in situ* hybridization in the small (A–D) and medium (E–H) size of the blastema. The dotted lines indicate the border of the blastema epithelium. Asterisks indicate the punctuated dermal collagen, indicating the amputation plane. Lines in A, C, E, and G indicate the approximate position of the longitudinal sections shown in B, D, F, and H. Scale bars in A and B = 200 μm. (I, J) *Shh* and *Fgf8* expression patterns in the medium size of the blastema in the 3D reconstructed image. The gray color shows the blastema mesenchyme. Posterior is to the left (A to J).

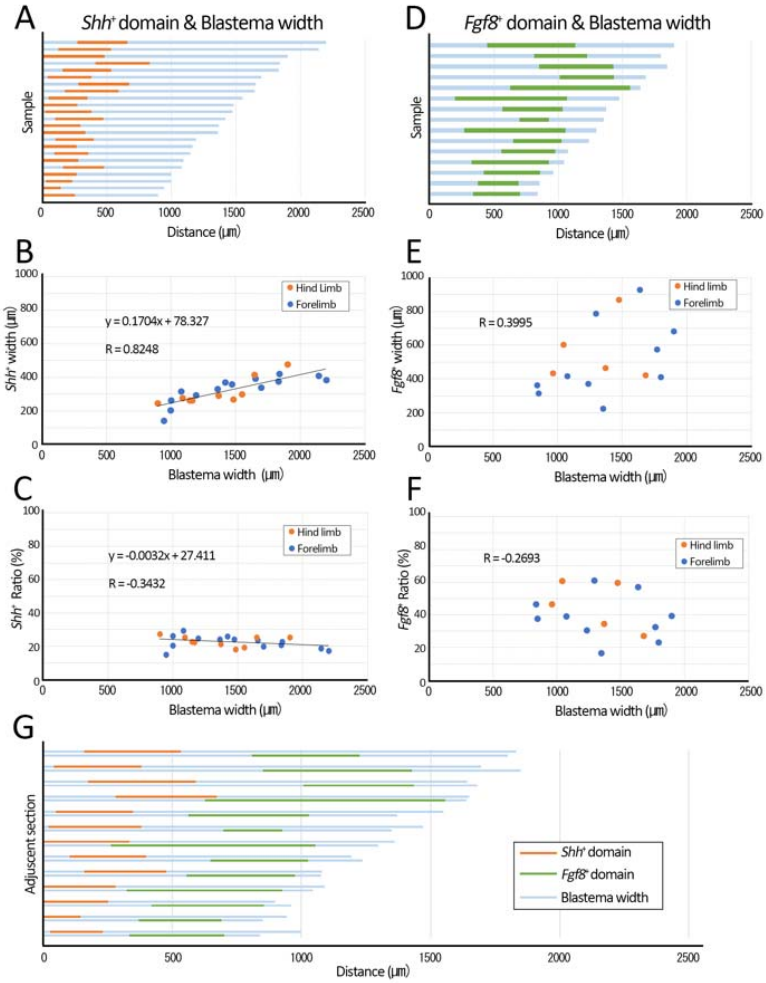

Fig. 3. Measurement of the *Shh*$^+$ and *Fgf8*$^+$ domain in blastemas. (A, D) The averaged width of the *Shh*$^+$ and *Fgf8*$^+$ domain collected from two to three sections is shown in orange and green, respectively. Blue indicates the width of the blastema mesenchyme along the anteroposterior axis. (B, E) The scatter plot illustrating the relationship between the width of the *Shh*$^+$ or *Fgf8*$^+$ domain and the blastema width. The line in B shows the collinear approximation represented by the formula. R shows the correlation coefficient. (C, F) The scatter plot illustrating the relationship between the ratio of the *Shh*$^+$ or *Fgf8*$^+$ domain in the blastema mesenchyme and the blastema width. The line in C shows the collinear approximation represented by the formula. R shows the correlation coefficient. (G) Two serial sections were prepared and *in situ* hybridization was performed on each series of sections to visualize the *Shh*$^+$ and *Fgf8*$^+$ cells. Each expression domain was measured and visualized in the same way as in (A) and (D). Only the samples that could be measured in the identical sample were extracted and shown.

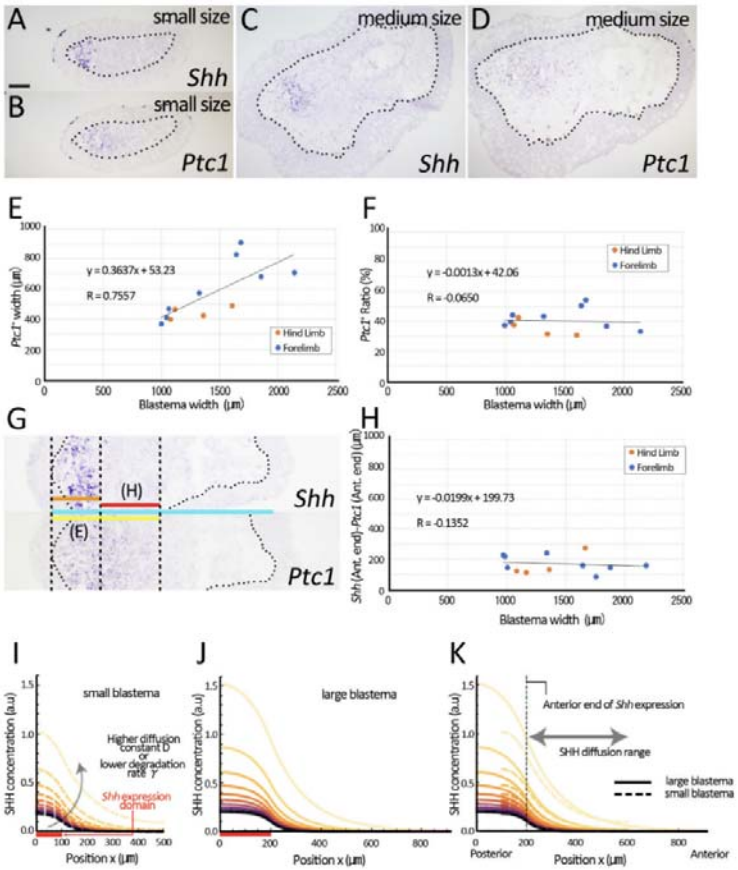

Fig. 4. *Ptc1* expression and assumptive SHH **distribution in blastemas.** (A–D) *Ptc1*or *Shh* expression was visualized by *in situ* hybridization. The dorsal is up and posterior to the left. Scale bar in A = 200 μm. The dotted lines indicate the border of the blastema epithelium. Posterior is to the left. (E–F) The scatter plot illustrating the relationship between the width or ratio of the *Ptc*$^+$ domain and the blastema width. The lines show the collinear approximation represented by the formula. R shows the correlation coefficient. (G) An explanation of the measurement for E and H. The red line indicates the SHH distribution, which was defined as the distance between the anterior borders of the *Shh*$^+$ and Ptc1$^+$ domain. (H) The scatter plot illustrating the relationship between the assumptive SHH distribution and the blastema width. (I–K) The graphs illustrate the results of simulations of SHH distribution in different widths of the *Shh*$^+$ domain. (I) The case of the smaller (100 μm, red line) *Shh*$^+$ domain. (J) The case of the larger (200 μm, red line) *Shh*$^+$ domain. (K) The merged images aligned with the anterior end of *Shh* expression. The lines with yellow to purple colors indicate the SHH concentration with different parameters in the diffusion constant (D) and the degradation rate (γ).

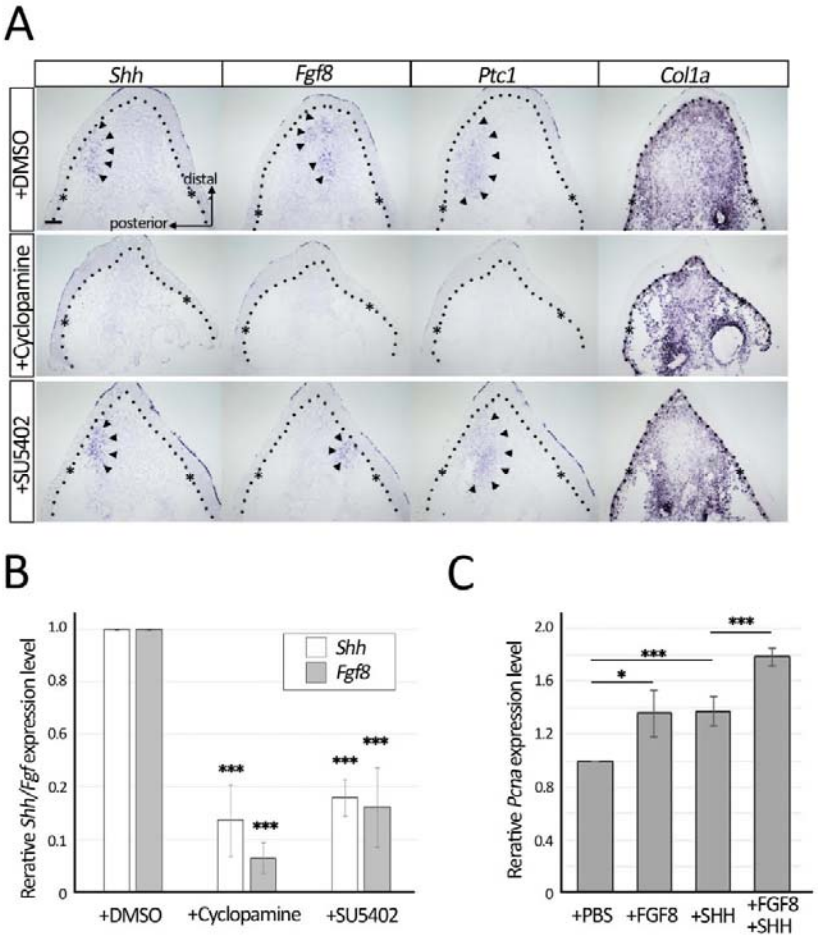

Fig. 5. Mutual dependence of *Shh* and *Fgf8* expression in regenerating blastemas. (A) *Shh*, *Fgf8*, *Ptc1*, and *Col1a* expression were visualized by *in situ* hybridization. The arrowheads indicate the localized expression. The asterisks indicate the punctuated derma collagen layer. The dotted lines indicate the border of the blastema epithelium. Scale bar = 200 μm. Posterior is to the left. (B) The relative expression level was measured by quantitative reverse transcription polymerase chain reaction (RT-PCR). The statistical analysis was performed using a two-tailed Student's *t*-test between the control and the samples. *p* values are represented as follows: ***< 0.01. (C) The relative *Pcna* expression level was measured by quantitative RT-PCR. The statistical analysis was performed using a one-way analysis of variance with Ryan's *post hoc* test. *p* values are represented as follows: ***< 0.01. *<0.05.

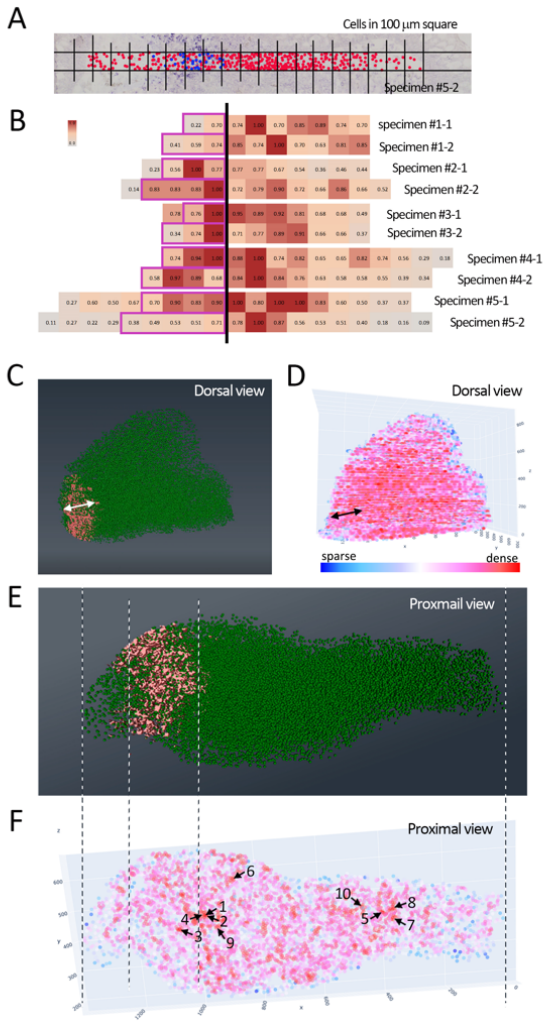

Fig. 6. Cell density in regenerating blastema. (A) Cell density and *Shh*$^{+}$ cells in a 100 µm squares were manually counted on the sections. Red and blue dots indicate cells/*Shh*$^{-}$ and cells/*Shh*$^{+}$, respectively. (B) The heatmap graph based on the count as in A. The number of cells in the square with the highest number of cells was set as 1, and the ratio was quantified. The purple boxes show the square containing *Shh*$^{+}$ cells. The bold black line indicates the anterior border of the *Shh*$^{+}$ domain. (C, E) The reconstituted image from the sections. The positions of the nuclei are shown in green, and the *Shh*$^{+}$ signal by *in situ* hybridization is shown in pink. (D, F) The heatmap illustrating cell density in a blastema. The double-headed arrows in C and D indicate the *Shh*$^{+}$ domain in the identical sample. (E, F) Three proximal sections were extracted and observed from the proximal side. Arrows and numbers in E indicate the 10 cells with the highest cell density from the visualized heatmap. Posterior is to the left (A to F).

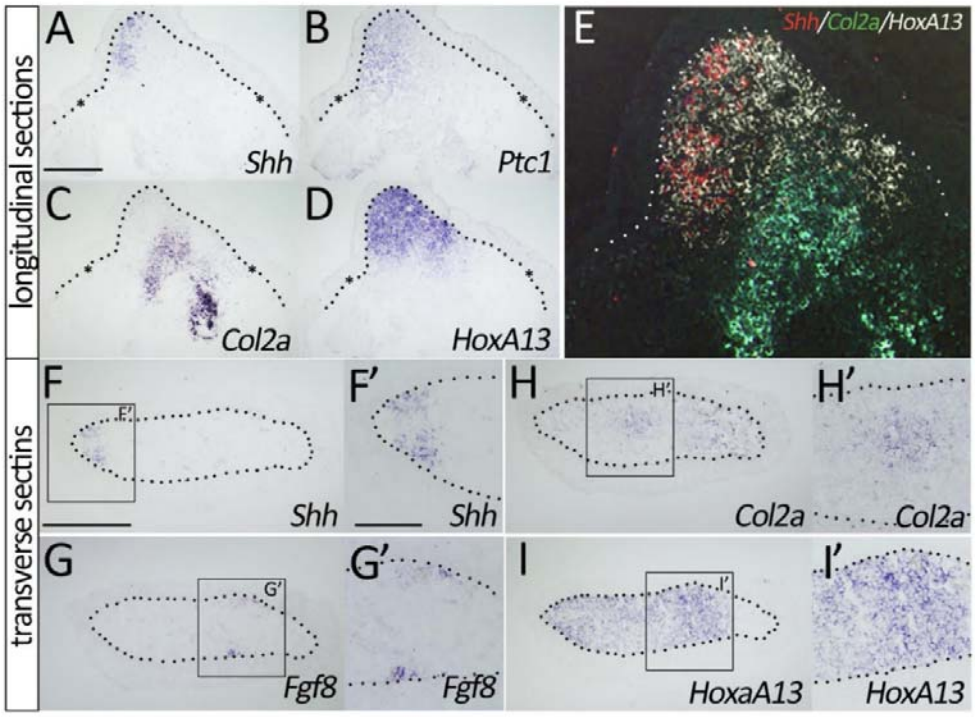

Fig. 7. First digit formation and *Shh* and *Fgf8* expression in the blastema at the first digit forming stage. (A–E) *Shh* (A), *Ptc1* (B), *Col2a* (C), and *HoxA13* (D) are visualized on longitudinal sections by *in situ* hybridization. The asterisks indicate the punctuated derma collagen layer. (E) Approximate merged illustration reconstituted from three adjacent sections. The locations of *Shh*$^+$ cells (red) and *Col2a*$^+$ cells (green) are projected onto the *HoxA13* (white) section. Scale bars in A = 500 μm. (F–I) *Shh* (F), *Fgf8* (G), *Col2a* (H), and *HoxA13* (I) are also visualized on the transverse sections. F'–I' are the higher magnification views of F–I. Scale bar in F = 500 μm. Scale bar in F' = 200 μm. The dotted lines indicate the border of the blastema epithelium. Posterior is to the left (A to I).

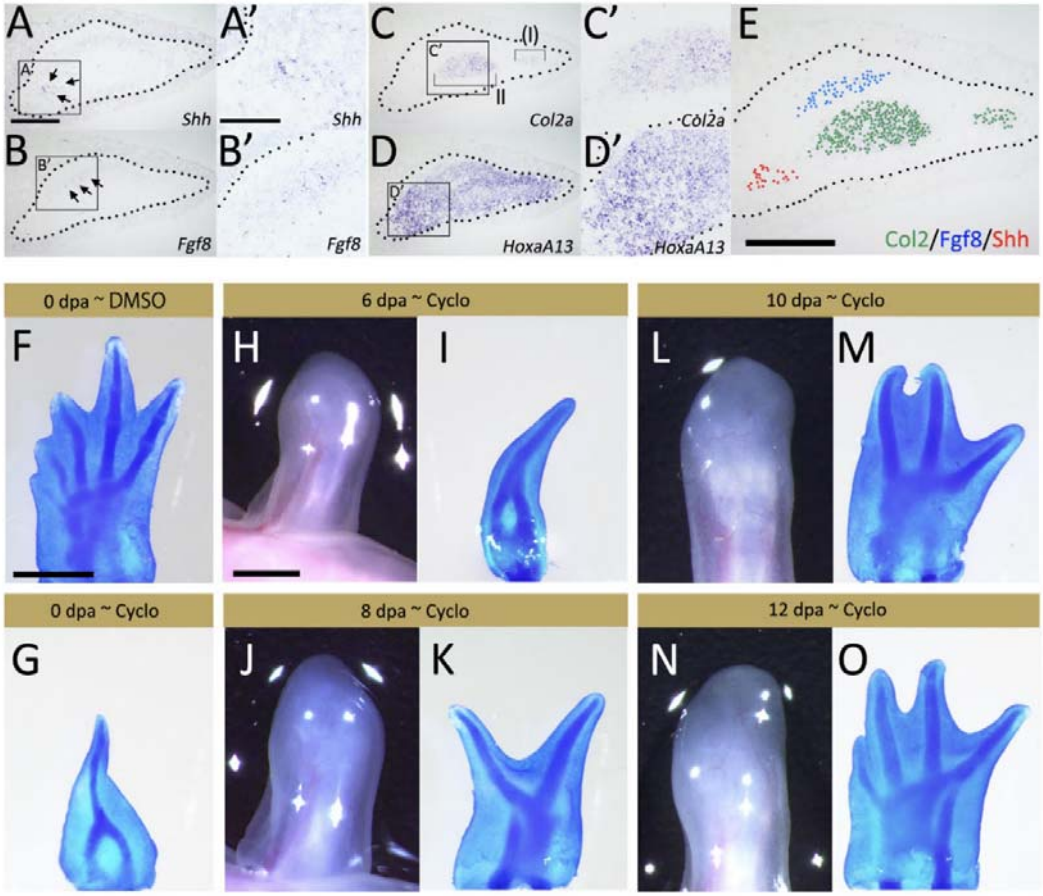

Fig. 8. Posterior digit formation and *Shh* and *Fgf8* expression in the blastema at the two-digit stage. (A–E) Gene expression pattern was investigated in the blastema prior to third digit formation. *Shh* (A, A'), *Fgf8* (B, B'), *Col2a* (C, C'), and *HoxA13* (D, D') were visualized by *in situ* hybridization. (E) Approximate merged illustration reconstituted from three adjacent sections. The locations of Shh^+ cells (red) and $Fgf8^+$ cells (blue) are projected onto the *Col2a* (green) section. Scale bars = 500 μm [(A, E)] and 250 μm [(A')]. The dotted lines indicate the border of the blastema epithelium. (F–O) Limb phenotypes produced by cyclopamine exposure with different treatment lengths. (F) Negative control (DMSO treatment). (G) The representative skeletal pattern, which had been treated from the beginning. (H, J, L, N) Blastema morphologies at the start of cyclopamine exposure. (I, K, M, O) Limb morphologies at the end of cyclopamine exposure. Scale bars = 1 mm [(F, H)]. Posterior is to the left (A to O).

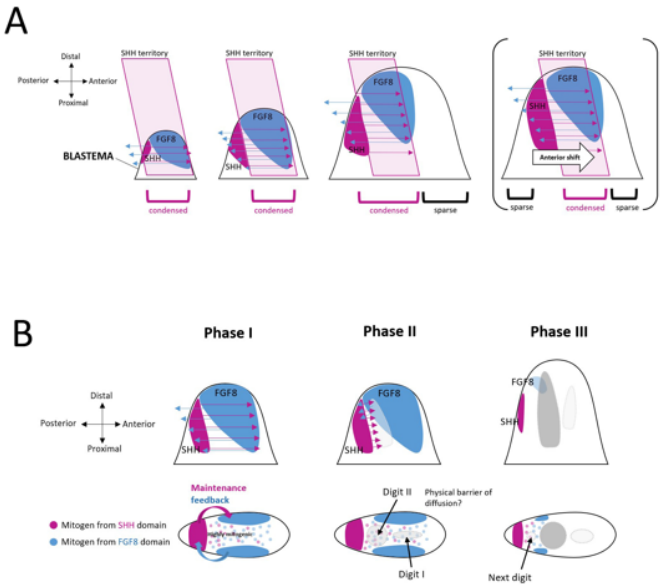

Fig. 9. Schematic diagram of the proposed limb patterning mechanism in axolotl limb regeneration. (A) SHH and FGF8, which are interdependent, are within their respective diffusion ranges in a small blastema. As a blastema becomes bigger, regions outside the diffusion range of SHH are produced. As the diffusion range of SHH is constant due to physiological characteristics, it is not affected by the size of the blastema. In a large blastema, the region of SHH-FGF8 is flexible. This inconsistent positioning arises from the inconsistent contribution of cells from anterior and posterior stump tissues to a blastema. The area under the influence from SHH and FGF8 shows higher mitogenic activity in a blastema. (B) A model of the anterior–posterior digit formation in an axolotl limb. Owing to the higher mitogenic activity in the area where they can receive both SHH and FGF8, cartilage differentiation is triggered in accordance with increasing cell density. In contrast, FGF8 also shows mitogenic activity. Thus, cartilage differentiation occurs slightly later in the anterior side flanked by FGF8. Differentiating cartilage should be rich in extracellular matrix and be a physical barrier to SHH and FGF8. Then, FGF8 is maintained in the small area, where SHH can be reached, resulting in the posterior shift of the SHH-FGF8 domain. Then, the next presumptive mitogenic point is formed between the shifted SHH and FGF8 domains. This sequence might explain urodele-specific anterior–posterior-ordered digit formation.

Table 1. Digit loss in cyclopamine-treated blastemas with different application times

Number of lost digit	0	1	2	3	4
0 dpa- cyclo. FL.				6	
0 dpa- cyclo. HL.					6
6 dpa-cyclo. FL.				6	
6 dpa-cyclo. HL.				3	3
8 dpa-cyclo. FL.			6		
8 dpa-cyclo. HL.				6	
10 dpa-cyclo. FL.	4	2			
10 dpa-cyclo. HL.			6		
12 dpa-cyclo. FL.	6				
12 dpa-cyclo. HL.	1	3	2		
0 dpa-DMSO FL.	6				
0 dpa-DMSO HL.	6				

Movie S1.

The spatial expression pattern of *Shh* (red) and *Fgf8* (blue). The image is reconstituted from the sections, in which gene expression was visualized by *in situ* hybridization.

Movie S2.

The distribution of nuclei (green) and *Shh*$^+$ cell (pink) in the blastema.

Movie S3.

The lateral view of the cell density visualized as the heatmap.

Movie S4.

The proximal view of the cells density visualized as the heatmap. To avoid a clouded image, the proximal three sections were selected and visualized.

Supplemental Fig. 1

The measurement of the gene expression domain. **(A and B)** The specific measurement method of *Shh* (A) and *Fgf8* (B). The light-blue lines indicate the length of the blastema mesenchyme (anteroposterior direction). The expression domain was indicated by orange (for *Shh*) and green (for *Fgf8*). The dotted lines indicate the border of the blastema epithelium. **(C and D)** The raw data of the *Shh*$^+$ (C) and *Fgf8*$^+$ (D) domain widths. The measurement was performed on 2-3 sections derived from an identical blastema. The lines indicate the results from all the measurement of 2-3 sections. The lines were bundled every blastema and displayed. (N=23 (*Shh*), N=15 (*Fgf8*)) The scale bar in A is 200 μm. Posterior is to the left.

References

1. Kragl M, *et al.* Cells keep a memory of their tissue origin during axolotl limb regeneration. *Nature* **460**, 60-65 (2009).

2. Hirata A, Gardiner DM, Satoh A. Dermal fibroblasts contribute to multiple tissues in the accessory limb model. *Development, Growth & Differentiation* **52**, 343-350 (2010).

3. Muneoka K, Sassoon D. Molecular aspects of regeneration in developing vertebrate limbs. *Dev Biol* **152**, 37-49 (1992).

4. Bryant SV, Endo T, Gardiner DM. Vertebrate limb regeneration and the origin of limb stem cells. *The International journal of developmental biology* **46**, 887-896 (2002).

5. Muneoka K, Bryant SV. Evidence that patterning mechanisms in developing and regenerating limbs are the same. *Nature* **298**, 369-371 (1982).

6. Gerber T, *et al.* Single-cell analysis uncovers convergence of cell identities during axolotl limb regeneration. *Science (New York, NY)* **362**, (2018).

7. Todd TJ. On the process of reproduction of the members of the aquatic salamander. *Quarterly Journal of Science, Literature and Arts* **16**, 84-96 (1823).

8. Makanae A, Mitogawa K, Satoh A. Co-operative Bmp- and Fgf-signaling inputs convert skin wound healing to limb formation in urodele amphibians. *Dev Biol* **396**, 57-66 (2014).

9. Satoh A, Makanae A, Nishimoto Y, Mitogawa K. FGF and BMP derived from dorsal root ganglia regulate blastema induction in limb regeneration in Ambystoma mexicanum. *Developmental Biology* **417**, 114-125 (2016).

10. Yamamoto S, Kashimoto R, Furukawa S, Sakamoto H, Satoh A. Nerve-mediated FGF-signaling in the early phase of various organ regeneration. *Journal of Experimental Zoology Part B: Molecular and Developmental Evolution* **n/a**.

11. Torok MA, Gardiner DM, Izpisúa-Belmonte JC, Bryant SV. Sonic hedgehog (shh) expression in developing and regenerating axolotl limbs. *The Journal of experimental zoology* **284**, 197-206 (1999).

12. Purushothaman S, Elewa A, Seifert AW. Fgf-signaling is compartmentalized within the mesenchyme and controls proliferation during salamander limb development. *Elife* **8**, (2019).

13. Nacu E, Gromberg E, Oliveira CR, Drechsel D, Tanaka EM. FGF8 and SHH substitute for anterior-posterior tissue interactions to induce limb regeneration. *Nature* **533**, 407-410 (2016).

14. Han MJ, An JY, Kim WS. Expression patterns of Fgf-8 during development and limb regeneration of the axolotl. *Developmental dynamics : an official publication of the American Association of Anatomists* **220**, 40-48 (2001).

15. Ohuchi H, Yoshioka H, Tanaka A, Kawakami Y, Nohno T, Noji S. Involvement of androgen-induced growth factor (FGF-8) gene in mouse embryogenesis and morphogenesis. *Biochem Biophys Res Commun* **204**, 882-888 (1994).

16. Crossley PH, Minowada G, MacArthur CA, Martin GR. Roles for FGF8 in the induction, initiation, and maintenance of chick limb development. *Cell* **84**, 127-136 (1996).

17. Xu X, Mackem S. Tracing the Evolution of Avian Wing Digits. *Current Biology* **23**, R538-R544 (2013).

18. Fröbisch NB, Shubin NH. Salamander limb development: Integrating genes, morphology, and fossils. *Developmental Dynamics* **240**, 1087-1099 (2011).

19. Nye HLD, Cameron JA, Chernoff EAG, Stocum DL. Extending the table of stages of normal development of the axolotl: Limb development. *Developmental Dynamics* **226**, 555-560 (2003).

20. Li Y, Zhang H, Litingtung Y, Chiang C. Cholesterol modification restricts the spread of Shh gradient in the limb bud. *Proceedings of the National Academy of Sciences* **103**, 6548 (2006).

21. Tickle C, Barker H. The Sonic hedgehog gradient in the developing limb. *WIREs Developmental Biology* **2**, 275-290 (2013).

22. Lewis PM, *et al.* Cholesterol modification of sonic hedgehog is required for long-range signaling activity and effective modulation of signaling by Ptc1. *Cell* **105**, 599-612 (2001).

23. Marigo V, Scott MP, Johnson RL, Goodrich LV, Tabin CJ. Conservation in hedgehog signaling: induction of a chicken patched homolog by Sonic hedgehog in the developing limb. *Development* **122**, 1225-1233 (1996).

24. Crossley PH, Minowada G, MacArthur CA, Martin GR. Roles for FGF8 in the induction, initiation, and maintenance of chick limb development. *Cell* **84**, 127-136 (1996).

25. Purushothaman S, Lopez Aviña BB, Seifert AW. Sonic hedgehog is essential for proximal-distal outgrowth of the limb bud in salamanders. *bioRxiv*, 2021.2009.2016.460693 (2021).

26. Purushothaman S, Elewa A, Seifert AW. Fgf-signaling is compartmentalized within the mesenchyme and controls proliferation during salamander limb development. *eLife* **8**, e48507 (2019).

27. Matsutani E, Kuroda Y. Effect of lectins on chondrogenesis of cultured quail limb bud cells. *Dev Biol* **89**, 521-526 (1982).

28. Roy S, Gardiner DM. Cyclopamine induces digit loss in regenerating axolotl limbs. *The Journal of experimental zoology* **293**, 186-190 (2002).

29. Stopper GF, Wagner GP. Inhibition of Sonic hedgehog signaling leads to posterior digit loss in Ambystoma mexicanum: parallels to natural digit reduction in urodeles. *Developmental dynamics : an official publication of the American Association of Anatomists* **236**, 321-331 (2007).

30. Robert B, Lallemand Y. Anteroposterior patterning in the limb and digit specification: Contribution of mouse genetics. *Developmental Dynamics* **235**,

2337-2352 (2006).

31. Farin HF, *et al.* Tbx2 terminates Shh/Fgf Signaling in the developing mouse limb bud by direct repression of Gremlin1. *PLOS Genetics* **9**, e1003467 (2013).

32. Matsubara H, Saito D, Abe G, Yokoyama H, Suzuki T, Tamura K. Upstream regulation for initiation of restricted Shh expression in the chick limb bud. *Developmental dynamics* **246**, 417-430 (2017).

33. Satoh A, Makanae A. Conservation of position-specific gene expression in axolotl limb skin. *Zoological science* **31**, 6-13 (2014).

34. Gardiner DM, Muneoka K, Bryant SV. The migration of dermal cells during blastema formation in axolotls. *Dev Biol* **118**, 488-493 (1986).

35. Iwata R, Makanae A, Satoh A. Stability and plasticity of positional memory during limb regeneration in Ambystoma mexicanum. *Developmental dynamics : an official publication of the American Association of Anatomists* **249**, 342-353 (2020).

36. Muneoka K, Fox WF, Bryant SV. Cellular contribution from dermis and cartilage to the regenerating limb blastema in axolotls. *Developmental biology* **116**, 256-260 (1986).

37. Pickering J, Towers M. Inhibition of Shh signalling in the chick wing gives insights into digit patterning and evolution. *Development* **143**, 3514-3521 (2016).